

pubs.acs.org/JACS Article

Dynamic Bubbling Balanced Proactive CO₂ Capture and Reduction on a Triple-Phase Interface Nanoporous Electrocatalyst

Wei Zhang, Ao Yu, Haiyan Mao, Guangxia Feng, Cheng Li, Guanzhi Wang, Jinfa Chang, David Halat, Zhao Li, Weilai Yu, Yaping Shi, Shengwen Liu, David W. Fox, Hao Zhuang, Angela Cai, Bing Wu, Fnu Joshua, John R. Martinez, Lei Zhai, M. Danny Gu, Xiaonan Shan, Jeffrey A. Reimer,* Yi Cui,* and Yang Yang*



Cite This: J. Am. Chem. Soc. 2024, 146, 21335-21347



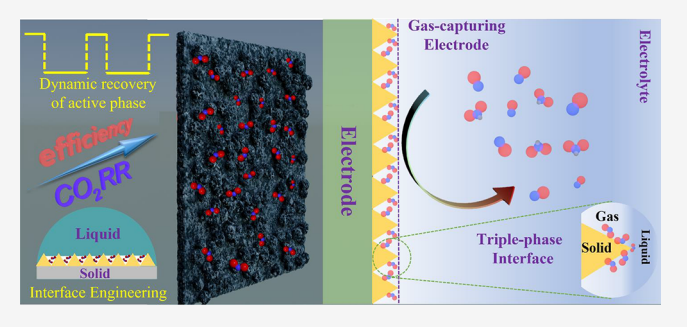
ACCESS I

Metrics & More

Article Recommendations

Supporting Information

ABSTRACT: The formation and preservation of the active phase of the catalysts at the triple-phase interface during CO2 capture and reduction is essential for improving the conversion efficiency of CO₂ electroreduction toward value-added chemicals and fuels under operational conditions. Designing such ideal catalysts that can mitigate parasitic hydrogen generation and prevent active phase degradation during the CO₂ reduction reaction (CO₂RR), however, remains a significant challenge. Herein, we developed an interfacial engineering strategy to build a new SnO_x catalyst by invoking multiscale approaches. This catalyst features a hierarchically nanoporous structure coated with an organic F-monolayer



that modifies the triple-phase interface in aqueous electrolytes, substantially reducing competing hydrogen generation (less than 5%) and enhancing CO₂RR selectivity (~90%). This rationally designed triple-phase interface overcomes the issue of limited CO₂ solubility in aqueous electrolytes via proactive CO2 capture and reduction. Concurrently, we utilized pulsed square-wave potentials to dynamically recover the active phase for the CO2RR to regulate the production of C1 products such as formate and carbon monoxide (CO). This protocol ensures profoundly enhanced CO₂RR selectivity (\sim 90%) compared with constant potential (\sim 70%) applied at −0.8 V (V vs RHE). We further achieved a mechanistic understanding of the CO₂ capture and reduction processes under pulsed square-wave potentials via in situ Raman spectroscopy, thereby observing the potential-dependent intensity of Raman vibrational modes of the active phase and CO₂RR intermediates. This work will inspire material design strategies by leveraging triplephase interface engineering for emerging electrochemical processes, as technology moves toward electrification and decarbonization.

1. INTRODUCTION

Promoting electroreduction of CO₂ to value-added chemicals and fuels is critically important for achieving global electrification and decarbonization targets by 2050. 1-3 The electrocatalytic CO₂ reduction reaction (CO₂RR) converts CO₂ gas into carbon-containing chemicals such as C₁ (carbon monoxide (CO), formic acid (HCOOH), methanol, methane, etc.), C_2 (ethylene, ethanol, acetate, ethylene glycol, etc.), and C_{2+} products (propanol, propionaldehyde, etc.), depending on the specific reaction pathways on the catalysts.⁴ Among the major products, C₁ products (particularly HCOOH and CO) are considered the most economically viable due to their high energy storage capacity and broad applications as building blocks in the chemical manufacturing industry.⁵ While promising, conventional catalysts for C₁ products, such as Pd, Bi, and Cu, are either prohibitively expensive or exhibit low selectivity, making them unsuitable for scalable usage. Apart from the low selectivity of the catalysts, a major challenge is devising an optimal solid-liquid-gas triple-phase interface that could enhance CO₂RR conversion efficiency by overcoming the limited CO₂ solubility (~0.034 M under ambient conditions) in aqueous electrolytes as well as flooding on the catalysts.^{6,7} In addition, diminished CO2RR activity over prolonged periods due to catalyst degradation and surface reconstruction greatly limits large-scale implementation. Thus, dissecting the structure-property relationships and exerting dynamic control of the surface-active phase will prove advantageous in improving the selectivity and durability of the CO₂RR catalysts.

Tin oxides (SnO_x) , being cost-effective, earth-abundant, and nontoxic materials, have recently been reported to have high selectivity toward HCOOH via a 2-electron transfer pathway in CO₂RR, attributed to the preferred intermediate of *OCHO

Received: February 24, 2024 July 7, 2024 Revised: Accepted: July 10, 2024 Published: July 25, 2024





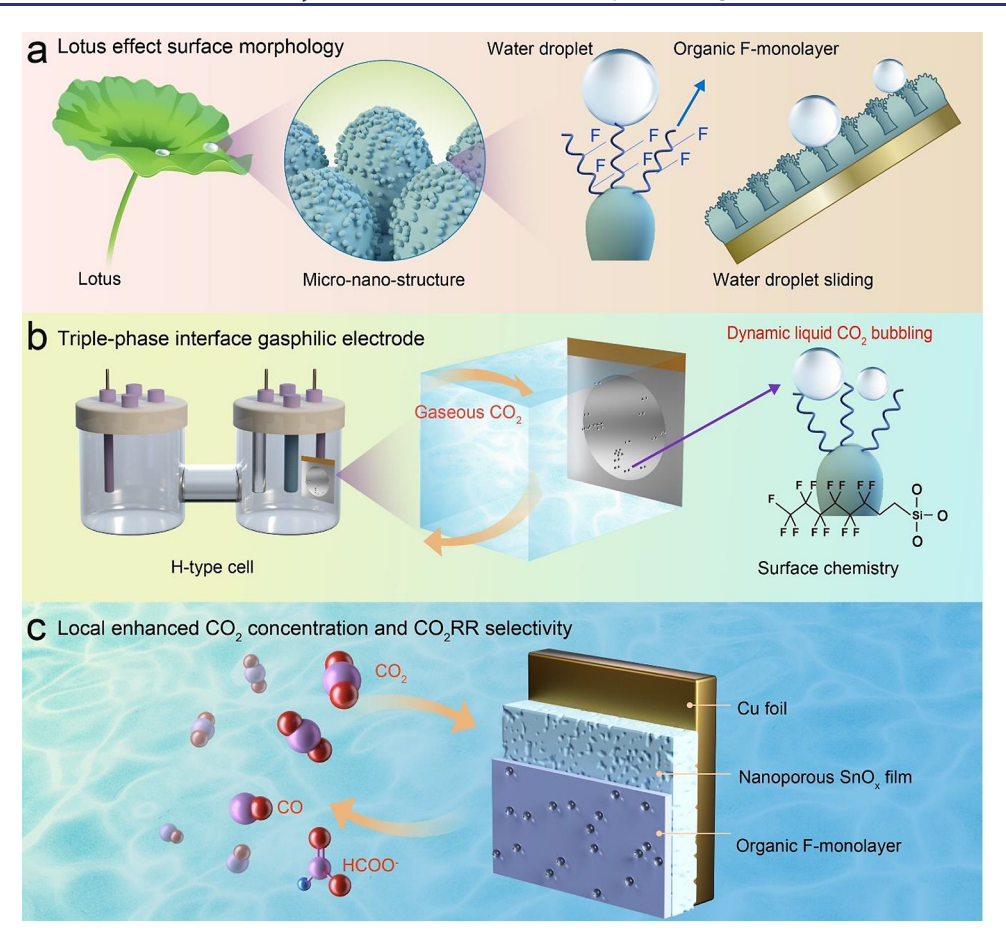


Figure 1. Schematics of the "lotus"-structured gasphilic SnO_x nanoporous film for CO_2 proactive capture and reduction.(a) Schematic illustration of "lotus" micronanostructure on a SnO_x nanoporous film coated with an organic F-monolayer and its superhydrophobic behavior; (b) schematic illustration of efficient dynamic liquid CO_2 bubbling enhanced the CO_2RR process in aqueous electrolyte on a triple-phase gasphilic interface; and (c) schematic configuration of BGPF electrode during the CO_2RR in aqueous electrolyte and reaction pathway.

formed due to its high oxygen affinity. Recent studies have focused on increasing active surface area of SnO_x by developing various nanostructures to facilitate mass and electron transfer for CO₂RR.⁸⁻¹² Nevertheless, a decrease in CO₂RR efficiency was observed when the oxide-based active phase was partially reduced to the metallic phase (i.e., surface reconstruction), which led to increased hydrogen generation, one of the most primary competing reactions and unresolved challenges in CO_2RR^{13-15} Like other oxide-based catalysts, SnO_x undergoes significant surface reconstruction and functional degradation in response to applied cathodic potentials. 16 These undesired atomic rearrangements and/or altered chemical states result in unstable and deactivated CO₂RR performance. ¹⁷ Hence, these deficiencies motivate key studies to understand the chemical transformation at the triple-phase interface microenvironment when designing oxide-based catalysts aimed at suppressing hydrogen generation and augmenting the conversion efficiency of dissolved CO₂ 18,19

One starting point for increased efficacy of CO_2RR catalytic reactions would be to enhance the gasphilicity of the catalysts, thereby improving CO_2 gas molecule mass transfer while maintaining alkaline reaction conditions. We note that natural materials, such as the lotus leaf, possess unique micronanostructures that support water droplets and trap air in their nanostructures. It is also clear that microenvironments at the triple-phase interface of the catalysts (e.g., CO_2 affinity, local electric field, exposure of active facets, etc.) can also be

optimized to favor CO₂RR.^{22,23} Finally, degradation of gasphilic behavior at the triple-phase interface is often encountered due to surface reconstruction of the catalysts under operational conditions²⁴ and could be improved.

Herein, we designed a bioinspired gasphilic SnO_x nanoporous electrode film that mimics a unique lotus surface structure to promote gasphilicity and thus increase local CO₂ concentration via a proactive CO₂-capturing process near the electrode surface. By invoking multiscale approaches, a favorable triple-phase interface for the CO2RR is created. We validated the concept that the CO₂RR selectivity can be significantly improved by further modifying the triple-phase interface via surface coating with a self-assembled organic F-monolayer (SAFM). Specifically, we recorded dynamic bubbling at the triple-phase interface while monitoring the surface chemical state changes of the electrode using in situ Raman techniques under square-wave pulsed potentials, facilitating a deeper mechanistic understanding of the structure-property relationship relevant for the CO2RR. We also verified the crucial role of dynamic recovery of the active phase in maintaining stable CO₂RR, specifically targeting the production of desired C1 products during long-term operation under pulsed potentials. The proposed interface engineering strategy precedes the regulation and preservation of electrochemical processes that are proposed for an electrified and decarbonized economy.

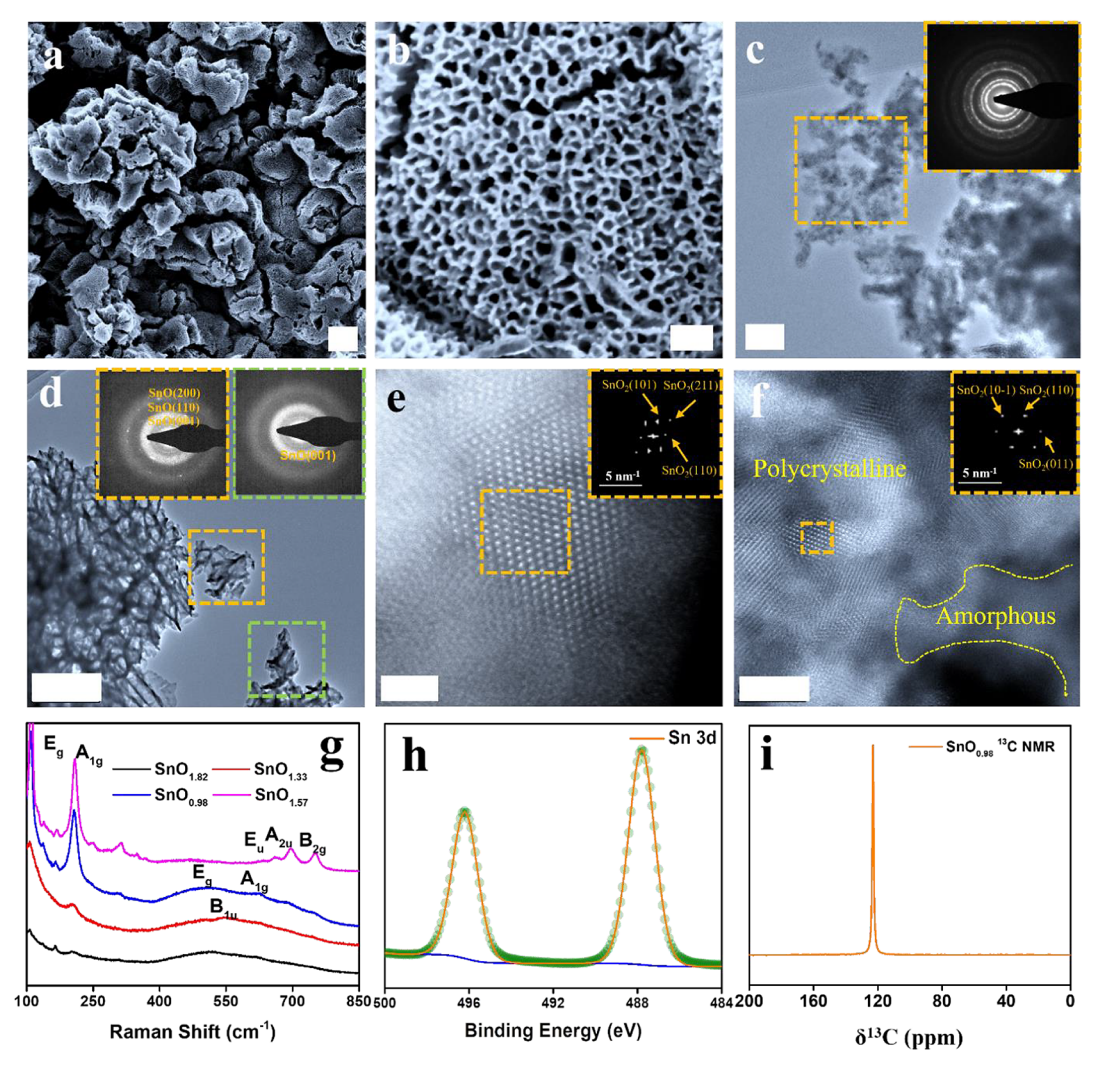


Figure 2. Structural characterization of thermal-driven phase modulation of hierarchically nanoporous SnOx films.(a) Top-view SEM image of the nanoporous structure. (b) Enlarged SEM image of the nanoporous structure. HAADF-STEM images of (c) SnO_{1.82}, (d) SnO_{1.33}, (e) SnO_{0.98}, and (f) SnO_{1.57}. (g) Raman spectra of SnO_{1.82}, SnO_{1.33}, SnO_{0.98}, and SnO_{1.57}. h, XPS Sn 3d spectrum of SnO_{0.98}. (i) Direct excitation ¹³C MAS (magic angle-spinning) NMR spectra of a CO₂-adsorbed SnO_{0.98} nanoporous film. Scale bars: (a) 1 μm, (b, c) 100 nm, (d) 200 nm, (e) 2 nm, and (f) 5 nm.

2. RESULTS AND DISCUSSION

2.1. "Lotus"-Structured Gasphilic Nanoporous Film **Electrode.** To mimic the unique lotus surface morphology and improve the gasphilic behavior of electrodes during CO₂RR, we developed a series of SnO_x electrode films with a hierarchically nanoporous morphology using electrodeposition and anodization, followed by thermal annealing and surface coating of SAFM (see the Supporting Information for detailed experimental procedures). The fabricated "lotus"-structured nanoporous electrode film featured micronanostructures that show incredible superhydrophobic behavior where water easily slides off the electrode (Figure 1a). We performed the CO₂RR in an H-type cell filled with a CO₂-saturated aqueous electrolyte. More surprisingly, the nanoporous film electrode shows a "plastron"-like triple-phase interface in the aqueous electrolyte, which enables dynamic CO2 bubbling balanced capture and reduction processes via a combination of morphology control and surface chemistry (Figure 1b). Moreover, this nanoporous film fabrication and configuration significantly improved CO₂RR selectivity toward CO and formate due to enhanced local CO₂ concentration, enabling faster mass transfer at the

triple-phase interface (Figure 1c). More details will be discussed in the following sections.

2.2. Thermal Treatment to Produce an Active Phase.

Tin oxides (SnO_x) exhibit higher oxygen affinity and CO₂RR activity compared to metallic Sn due to their unique chemical structure, which stabilizes *CO₂^{-.25} However, it remains elusive how the stoichiometry of Sn and O in SnO_x influences CO_2RR selectivity toward the production of CO and formate. 15,26 In general, different stoichiometric ratios in SnOx lead to different material properties due to the contrasting intrinsic semiconductor characteristics of p-type SnO and n-type SnO₂, quantities of which can be altered via thermally induced phase transformation.^{27,28} The sample just after anodization was denoted SnO_{1.82}. Thermally annealing the anodized samples at 200, 300, and 450 °C yielded samples denoted SnO_{1,33}, SnO_{0,98}, and SnO_{1,57}, respectively. The stoichiometric ratios between Sn and O for all samples were determined by scanning transmission electron microscopy-energy-dispersive X-ray spectroscopy (STEM-EDS) mapping. Our results indicate that the most effective SnO_x for CO₂RR comprises of amorphous SnO and polycrystalline SnO₂ in SnO_{0.98}, to be discussed below.

The micronanostructures of the SnO_x catalysts were examined by top-view scanning electron microscopy (SEM). For example, approximately 20 nm nanopores are shown to be uniformly distributed on the film electrode (Figure 2a,b). A cross-sectional SEM image of BGPF reveals a 4 μ m-thick SnO_x nanoporous layer grown on Cu foil (Figure S1). These micrographs reveal a hierarchically nanoporous structure that we surmise enables gas trapping at the triple-phase interface for the CO₂RR. Transmission electron microscopy (TEM) was utilized to reveal the thermodynamic phase composition of SnO_x nanoporous films annealed at different temperatures. The surface layers of the samples were analyzed instead of the bulk to prevent potential damage to the nanoporous framework from the energetic e-beam used in TEM. Therefore, all the crystal lattice and phase information presented below pertains to the top nanoporous layer of the film. For original and annealed samples, stoichiometric ratios between oxygen and tin were detected by energy-dispersive spectroscopy (EDS) elemental analysis. As previously mentioned, during thermal treatment, the surface of the nanoporous film undergoes a phase transformation. The original SnO_{1.82} was found to have a polycrystalline SnO₂ structure, as indicated by the diffraction pattern, and is characterized by a stoichiometric ratio of 1.82 between O and Sn, as detected by energy-dispersive X-ray spectroscopy (EDX) elemental analysis. This suggests that the surface layer of the anodized sample consists of the crystallized SnO₂ phase and an amorphous SnO phase (Figures 2c and S2). Upon annealing at 200 °C, SnO_{1.82} was found to transform into SnO_{1.33}, indicating the formation of a new polycrystalline SnO phase alongside the SnO₂ and amorphous SnO phases. This transformation is confirmed by high-angle annular dark-field imaging-scanning transmission electron microscopy (HAADF-STEM) images and the diffraction patterns labeled for the (110), (012), $(10\overline{2})$, and (101), (200), (10 $\overline{1}$) planes for SnO and SnO₂, respectively (Figures 2d and S3). The newly formed crystalline SnO phase is likely crystallized from the amorphous phase through thermal annealing. Moreover, $SnO_{1.33}$ was further transformed into $SnO_{0.98}$ by increasing the annealing temperature to 300 °C. Note that the decreased oxygen content from 1.83 to 0.98 is attributed to the thermally driven migration of surface oxygen to the bottom bulk area of the film. ^{29,30} The 300 °C annealed SnO_{0.98} material exhibits an oxygen-deficient phase composition consisting of the amorphous phase and polycrystalline SnO₂, as determined from the diffraction pattern of (101), (211), and (110) planes of SnO₂ (Figure 2e). Moreover, the local interplanar spacing of 0.214 nm was assigned to SnO_2 (210) (Figure S4).³¹ Upon further annealing to 450 °C, the resulting SnO_{1.57} material displays a coexistence of the amorphous SnO phase and crystalline SnO₂ (Figure 2f), as identified by HAADF images (Figure S5). The deliberate thermally driven phase transformations allow for modulation of the oxygen-deficient SnO_{0.98} phase to obtain a modified triple-phase interface for efficient CO₂RR (vide infra).

X-ray diffraction (XRD) was also conducted to further examine the bulk structures of all of the nanoporous films (Figure S6). Broad diffraction peaks of amorphous SnO_x ($2\theta = 20-40^\circ$) were identified in $\mathrm{SnO}_{1.82}$, $\mathrm{SnO}_{1.33}$, and $\mathrm{SnO}_{0.98}$, indicating gradual phase transformations driven by thermal treatment at different temperatures. Prior to annealing, except for strong diffraction peaks from the substrate (Cu and Sn), $\mathrm{SnO}_{1.82}$ did not exhibit any clear peaks. Conversely, $\mathrm{SnO}_{1.33}$ shows a $\mathrm{SnO}(112)$ peak located at $\mathrm{50.7}^\circ$ (JCPDS 6-395), indicating the formation of a new phase after annealing.

Compared with SnO $_{1.33}$, SnO $_{0.98}$ displays additional SnO phases indicated by (101) and (002) diffractions at 29.8° and 37.1°, respectively, suggesting more crystalline SnO bulk phases formed at 300 °C. However, at a higher annealing temperature of 450 °C, the phase transformations culminate in the appearance of three broad peaks at 26.6°, 33.8°, and 51.7°, corresponding to SnO $_2$ (110), (101), and (211), respectively (JCPDS No. 41-1445). The other labeled Sn and Cu XRD peaks in the samples are derived from the electrodeposited Sn and substrate.

Raman spectroscopy was used to probe the vibrational mode of the lattice structures (Figure 2g). SnO_{1.82} exhibits a dominant broad vibrational peak centered at 514 cm⁻¹, suggesting a majority of the amorphous phase, with other vibrational peaks being less pronounced. SnO_{1,33} features two broad but less intense peaks around 100 and 210 cm^{-1} , which correspond to E_g and A_{1g} modes of the crystalline SnO phases, but a broad peak centered at 544 cm⁻¹ indicates the amorphous phase remains dominant.³² By contrast, SnO_{0.98} displays sharper and more intense Eg and Alg peaks compared to SnO_{1.33}, indicating the formation of the SnO crystalline phase. The broad peaks spanning 482 cm⁻¹ (E_g), 544 cm⁻¹ (B_{1u}), and 623 cm⁻¹ (A_{1g}) represent the transformation of lattice vibrations. However, more intense and sharper peaks located at 110 cm⁻¹ (E_g), 210 cm $^{-1}$ (A_{1g}), 659 cm $^{-1}$ (E_u), 696 cm $^{-1}$ (A_{2u}), and 752 (B_{2g}) cm $^{-1}$, were found in SnO_{1.57}, indicating a transformation from an amorphous structure to a more crystalline phase.³³ The Raman spectra are consistent with the XRD results in revealing the bulk phase transformation in the samples, suggesting a successive phase transformation as the annealing temperatures increases.

X-ray photoelectron spectroscopy (XPS) was utilized to identify the chemical states of the elements in the nanoporous films. The XPS Sn 3d spectrum (Figure 2h) of SnO_{0.98} shows 3d_{5/2} and 3d_{3/2} peaks at binding energies (BE) of 487.1 and 495.6 eV, respectively. These values can be assigned to nonstoichiometric tin oxides (SnO_x), implying a mixture of chemical states in the sample, aligning with XRD and Raman results.³⁴ The XPS O 1s spectrum (Figure S7a) shows BE of 530.7 and 532.2 eV that can be assigned to lattice oxygen and adsorbed hydroxy groups, respectively.³⁵ After surface functionalization with a self-assembled F-contained monolayer (SAFM), XPS survey spectra of SnO_{0.98}-F display the presence of fluorine as compared with SnO_{0.98} (Figure S8), successful linkage of SAFM to the sample via Si-O bonds is confirmed through deconvolution of XPS Si 2p and F 1s spectra at BE of 103 and 688.5 eV, respectively (Figure S7b,c). Moreover, the detection of -CF₃ (294.4 eV) and -CF₂ (291.8 eV) functional groups from XPS C 1s spectra (Figure S7d) further confirms the existence of SAFM, which plays a key role in interface engineering of the sample, contributing to repulsion between water and F-containing molecules during CO₂RR.³⁶ In addition to this repulsion, the CO2 molecules exhibit physisorption on the nanoporous film, suggesting enhanced CO₂ capture capacity within the nanoporous structure of the film, as evidenced by the direct 13C NMR spectrum of 13CO2-dosed SnO0,98-F, which shows a significant resonance at 123.0 ppm (Figure 2i).

2.3. Enhanced CO₂ Capture at "Plastron"-like Triple-Phase Interface. Biomaterials found in organisms such as insects and spiders facilitate underwater breathing by utilizing rough and hairy skin that can trap dissolved oxygen in the "plastron" layer. ^{37–39} Drawing inspiration from these creatures, we attempted control of the catalyst interface via a self-assembled coating to construct an artificial "plastron"-like

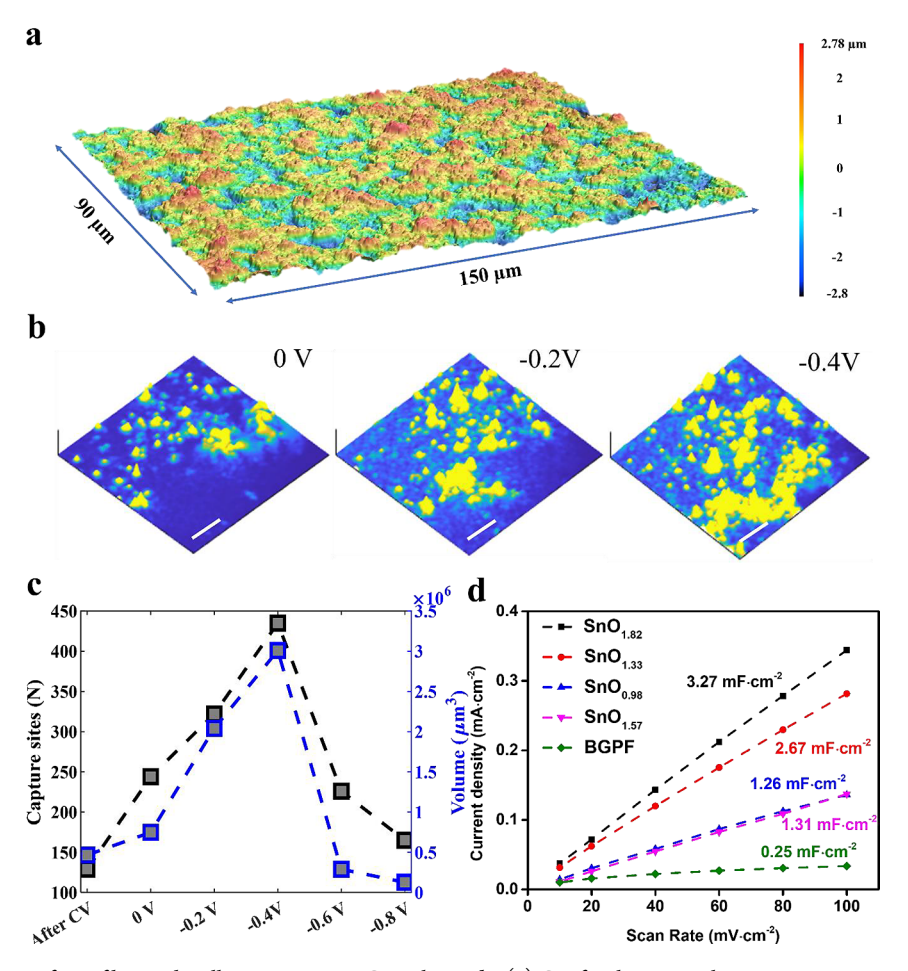


Figure 3. "Plastron"-like interface of hierarchically nanoporous BGPF electrode. (a) Confocal scanning laser microscopy image demonstrating surface morphology. (b) Surface morphological images of the BGPF electrode during CO_2 bubbling under constant potentials at 0, -0.2, and -0.4 V during the CO_2RR (scale bar: $40~\mu m$). (c) CO_2 -capturing properties of the BGPF electrode in a CO_2 -saturated 0.5 M KHCO $_3$ electrolyte: quantification of potential-dependent CO_2 -capturing sites and volume variance. (d) Calculated capacitance plotted against CV scan rates for different samples, derived from non-Faradaic current.

interface (Figure S9). This design enables gas trapping capabilities and increases the local CO₂ concentration near the electrode surface of SnO_{0.98}-F. Note that the term "bioinspired gasphilic nanoporous film" (BGPF) is used in the following discussion to represent the "plastron"-like interface of SnO_{0.98}-F. All non-SAFM-coated control samples were referred to as non-BGPF for easy comparison. Confocal laser scanning microscopy (Figure 3a) shows the "trough-ridge" surface topology of the BGPF electrode, indicative of a rough surface morphology with a surface roughness of 0.91 \pm 0.12 μ m and a maximum height of $6.23 \pm 0.9 \mu m$ (Figure S10). An advantage of the thermal treatment is the removal of the surface hydrophilic groups that remained within the nanoporous structure of BGPF after electrochemical synthesis. Evidence for the thermal removal of surface hydrophilic groups came from the reduced amount of hydroxyl group on BGPF (23.7%) compared with non-BGPF SnO_{1.82} (29.1%), as shown by the XPS O 1s spectra (Figure S11). Contact angle (CA) measurements also support hydroxyl group removal, as the BGPF shows superior hydrophobic properties with a largest CA of 158° compared to non-BGPF (Figure S12).

The effect of microstructure, surface roughness, and SAFM surface-coating on the hydrophobic properties was also studied. As depicted in Figure S12, it is evident that the $SnO_{0.98}$ sample annealed at 300 °C exhibits the largest CA in comparison to the

other annealed samples (SnO_{1.33} and SnO_{1.57}) and the unannealed SnO_{1.82}. However, as shown in Figure S13, the surface morphologies of the original sample (SnO_{1.82}) without annealing, the annealed samples $(SnO_{1.33})$ and $SnO_{1.57}$ and BGPF are highly similar. This suggests that the microstructure of the samples could not significantly affect the hydrophobicity properties. The surface roughness data for all samples are provided in Figures S14 and S15, showing variations in surface roughness among the samples. For the samples without SAFMcoating, surface roughness initially drops sharply and then gradually increases as the annealing temperature rises from 200 to 450 °C. This can be attributed to the gradual changes in the elemental composition of the SnOx layer. After coating the samples with SAFM, the roughness trend of the SAFM-coated samples is similar to that of the samples without SAFM-coating. Considering the CA data in Figure S12, it is evident that the roughness of the samples without SAFM-coating significantly affects their hydrophobicity. Enhanced hydrophobicity was achieved in the SnO_{0.98} sample, which exhibited suitable roughness. Notably, for the SAFM-coated samples, although the CA values for SnO_{1.82}-F, SnO_{1.33}-F, and SnO_{1.57}-F are significantly improved, they remain lower than that of SnO_{0.98} (BGPF). The primary factors influencing hydrophobicity are surface roughness and SAFM-coating. In addition, sliding behavior experiments in Video S1a,b show that water droplets

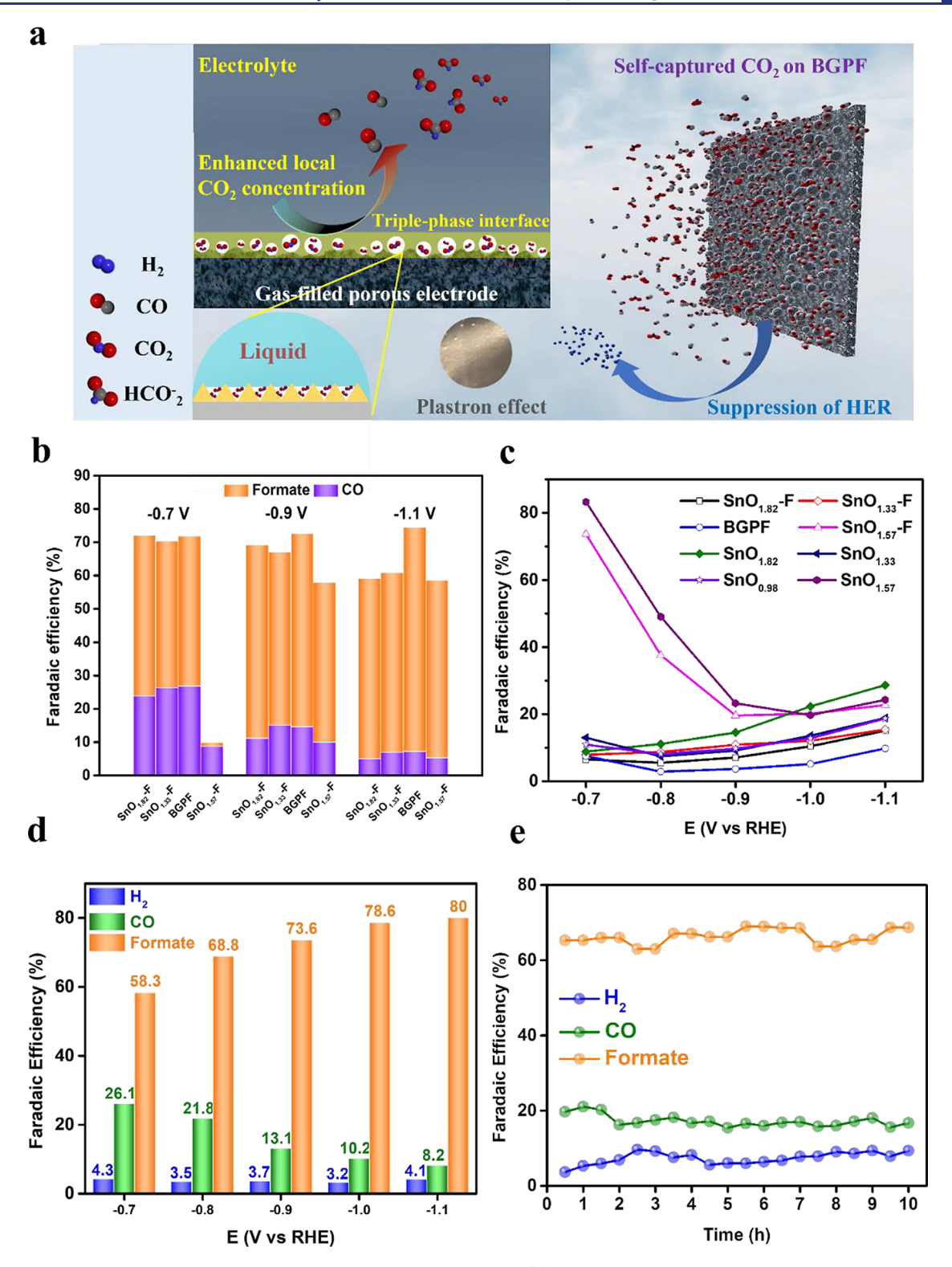


Figure 4. Electrochemical performance of hierarchically nanoporous SnO_x films. (a) Schematic illustration providing a mechanistic understanding of efficient CO₂RR on the gas-capturing BGPF electrode. (b) The CO₂RR Faradaic efficiency (FE) of BGPF, SnO_{1.82}-F, SnO_{1.83}-F, and SnO_{1.57}-F electrodes under different constant potentials. (c) Comparison of HER FE of the nanoporous films under different constant potentials during the CO₂RR. (d) The CO₂RR FE of the BGPF electrode in pulsed conditions at different potentials ($\Delta t_c = 60$ and $\Delta t_a = 5$ s, applied cyclically). (e) The CO₂RR FE of the BGPF electrode under pulsed electrochemical conditions ($\Delta t_c = 60$ s at -0.8 V and $\Delta t_a = 5$ s at 0.2 V, applied cyclically) during a 10 h stability test.

can easily slide off the BGPF electrode, demonstrating the water-repellent and gasphilic features of the electrode.

To visually probe the electrode—electrolyte interactions at the triple-phase interface of the nanoporous films, we utilized an

underwater camera to record the solid—liquid—gas interface near the electrode during the CO₂RR in a CO₂-saturated electrolyte. We compared the surface state of the gasphilic BGPF with that of the superhydrophilic non-BGPF electrode. Figure

\$16a reveals gas bubbles confined in the nanoporous structure of the BGPF electrode, a result of the "plastron" effect. However, the non-BGPF electrode shows no signs of gas bubble affinity (Figure S16b), thereby verifying that the gasphilic nature of the BGPF electrode aids in gas capture and enhances the local CO₂ concentration. In particular, we captured videos displaying the dynamic states of surface bubbling on the BGPF electrode under various constant potentials underwater and analyzed the bubble nucleation and growth processes. Figure 3b illustrates the changes in the surface morphology images during the CO2 capture under different applied potentials. There is a noticeable increase in dynamic bubbling from 0 to -0.4 V. We also calculated and compared the number of estimated capture sites and volumes of CO₂ bubbles per unit area captured at various potentials (Figure S17). Following a cyclic voltammetry (CV) scan to clean and activate the electrode, different constant potential windows were scanned (0, -0.2, -0.4, -0.6, and -0.8V). The corresponding numbers of bubble capture sites were obtained, validating the potential-dependent nature of the bubble capture and nucleation processes (Figure S18). As shown in Figure 3c, prior to reaching a voltage of -0.4 V vs RHE, the bubble-capturing process exhibits progressively enhanced peaks as the applied voltage becomes more negative. Notably, the bubble-capturing peaks at around -0.4 V, after which it begins to diminish as the potential further decreases, suggesting the uninterrupted consumption of some captured CO₂ molecules by CO₂RR beyond -0.4 V. These observations imply that the nucleation and growth of CO₂ bubbles on the BGPF electrode predominantly occur between voltages of 0 to -0.4 V, whereas CO₂ reduction becomes the dominant process as the voltage ranges from -0.4 to -0.8 V. Remarkably, the dynamic process of CO2 nucleation and bubbling was revealed in Video S3, showcasing the CO₂ self-capturing process on the BGPF electrode following a CV scan conducted under various potentials. Variations in the CO₂ bubbling rates were observed in the series of videos following frame subtraction, confirming the CO₂ self-capture process. In contrast, the superhydrophilic non-BGPF electrode shows a negligible change in surface bubbling states (Video S4), emphasizing the importance of the surface coating in our proposed interface engineering. The effective CO₂ capturing process, as described above, critically influenced the local microenvironment near the electrode surface. This insight not only sheds light on novel electrode designs for efficient triple-phase interface engineering, but also provides a solution to the challenge of limited CO₂ solubility when carrying out CO₂RR in aqueous solutions.

We examined the relationship between the electrochemically active surface area (ECSA) and the gasphilicity of the samples, confirming the critical role of our proposed interface engineering in tuning the local microenvironment. 40,41 Figure 3d shows the electrochemical double-layer capacitance of the nanoporous films calculated from CV tests (Figure S19). This measure correlates proportionally with the ECSA, which reflects the surface area wetted by the electrolyte. Among all samples, the BGPF electrode demonstrates the lowest capacitance of 0.25 mF/cm², owing to the "plastron" effect at the engineered triplephase interface. An efficient triple-phase interface has a relatively low ECSA because gas bubbles encapsulated at the surface prevent the electrolyte from inundating the electrode. Thus, the triple-phase interface of BGPF suggests a significantly improved local CO₂ concentration and microenvironment that may promote the CO₂RR. In contrast, non-BGPF SnO_{1.82} shows the highest capacitance among the samples of 3.27 mF/cm², due

to increased contact between the electrode and electrolyte, possibly resulting in heightened competition between the hydrogen evolution reaction (HER) and the $\rm CO_2RR$. The non-BGPFs $\rm SnO_{1.33}$, $\rm SnO_{0.98}$, and $\rm SnO_{1.57}$ display intermediate capacitances of 2.67, 1.26, and 1.31 mF/cm², respectively. These measurements reflect varying interfacial properties induced by phase transformation, confirming that the unique gasphilic morphology and surface coating of the samples improve the microenvironment at the triple-phase interface.

To further understand how the gasphilicity of the BGPF electrode affects the microenvironment at the triple-phase interface, where CO2 gas has a strong affinity to the solid electrode, we performed an analogous study of the oxygen evolution reaction (OER) process, comparing the gas-evolving properties of a sample with a hierarchically nanoporous surface and a sample with a flat surface. As shown in Figure S20, we compared linear sweep voltammetry (LSV) and chronopotentiometry curves for the OER on the BGPF electrode, non-BGPF electrode, and flat SnO_x electrode. The BGPF electrode shows a significantly lower current density of 12.0 mA/cm² at a potential of 2.0 V in the LSV curve, compared to the non-BGPF electrode (50.7 mA/cm² at 2.0 V) and flat SnO_x electrode (60.4 mA/cm² at 2.0 V). This result suggests that the captured gas in the BGPF electrode limits contact area between the electrode and electrolyte. Furthermore, the BGPF electrode exhibits an unstable and fluctuating i-t curve at a constant current density of 5 mA/cm² caused by the accumulation of generated gas bubbles on the surface of the BGPF electrode. This provides additional evidence of enhanced gas capture capability of the electrode and an increased affinity of the gas bubbles to the electrode.42

2.4. Improved CO₂RR at Modified Triple-Phase Inter**face.** Herein, we demonstrate the effectiveness of the rationally designed BGPF that has a modified triple-phase interface for CO₂RR conversion to C₁ products (e.g., CO and formate).⁴³ Figure 4a schematically depicts the function and CO₂RR reaction mechanism of the BGPF electrode. We find that the modified triple-phase interface can efficiently and proactively capture and subsequently reduce CO2 in a CO2-saturated aqueous medium due to its gasphilic characteristics that are known collectively as the Cassie state. 44 This process suppresses the parasitic generation of hydrogen by repulsion of water molecules from the electrode surface, thus improving the conversion efficiency of CO₂RR against HER.⁴⁵ The schematically depicted CO₂RR process is explicitly observed in Video S2, in which the saturated CO2 molecules dissolved in the electrolyte are self-captured by the electrode, followed by nucleation, growth, and bubbling.

The electrocatalytic CO_2RR performance of the samples was evaluated in an H-type cell filled with the CO_2 -saturated 0.5 M KHCO₃ electrolyte. All voltages are in reference to the reversible hydrogen electrode (RHE). CV was utilized to record the oxidation and reduction peaks of the samples, revealing two broad anodic and cathodic peaks in the CO_2 -saturated electrolyte. Conversely, in the N_2 -saturated electrolyte solution, two sets of clear anodic and cathodic peaks were observed at 0.15 and -0.25 V. These peaks correspond to the oxidation of Sn^0 to $Sn^{2+/4+}$ and reduction of $Sn^{2+/4+}$ to Sn^0 , respectively (Figure S21), suggesting the presence of a mixed phase in $SnO_{0.98}$. Chronoamperometry (Figure S22) was conducted to study the Faradaic efficiency (FE) and current density of the CO_2RR at different potentials. The gaseous and liquid products were analyzed through gas chromatography (GC, Figure S23)

and ¹H nuclear magnetic resonance (NMR, Figure S24), respectively. After coating SAFM on the surface of the samples, the BGPF electrode demonstrates the CO₂RR with a partial current density of 5.7 mA/cm² at −1.1 V, a performance that exceeds all other control samples in this work (Figure S25a). To unravel the impact of the SAFM-coating on the electrode surface, we also investigated the CO₂RR in samples without SAFM-coating. Decreased performance was also observed for the non-BGPF electrodes with CO₂RR partial current densities of 4.3, 2.9, 3.7, and 4.1 mA/cm² for SnO_{0.98}, SnO_{1.82}, SnO_{1.33}, and SnO_{1.57}, respectively (Figure S25b). However, the SAFM-coated samples exhibit higher CO₂RR partial current densities than their counterparts without the SAFM-coating, implying that the coating modifies the microenvironment, reducing the non-CO₂RR faradaic current.

We also compared the CO_2RR selectivity of BGPF and other control electrodes (e.g., $SnO_{1.82}$ -F, $SnO_{1.33}$ -F, and $SnO_{1.57}$ -F) at constant potentials of -0.7, -0.9, and -1.1 V, as shown in Figure 4b. The BGPF electrode shows a CO production FE of 26.3, 14.3, and 6.7%, accompanied by a formate production FE of 55.1, 68.2, and 77.5% at -0.7, -0.9, and -1.1 V, respectively, surpassing all other SAFM-coated control samples. Note that the $SnO_{1.57}$ -F sample shows much lower FE for CO and formate (8.5, 9.7, and 5.1% for CO and 10.1, 58, and 63% for formate at -0.7, -0.9, and -1.1 V, respectively), implying suboptimal CO_2RR performance due to the unsuitable mixed phase present in the sample even with SAFM-coating. This observation underscores the significance of thermally driven phase transformation in improving the CO_2RR selectivity.

To validate the significance of the unique nanoporous morphology endowed by our proposed interface engineering, we conducted tests on a flat SnO_x film electrode (Figure S26). The drastic decrease in total CO₂RR efficiencies (less than 50%) across all potentials suggests that the parasitic HER tends to overshadow the CO₂RR electrochemical processes. This result highlights the key role of morphology control in the suppression of HER. We also observed that all SAFM-coated samples demonstrated better CO2RR selectivity than their uncoated counterparts (Figure S27), reaffirming the importance of SAFM in enhancing the CO2RR selectivity due to further increase in gasphilicity at the triple-phase interface. 46 Among these samples, BGPF shows the highest CO₂RR FE of 84.2% with a partial current density of 5.7 mA/cm² at -1.1 V. This further confirms that the synergistic combination of morphology control and surface coating can improve the CO2RR performance at the modified triple-phase interface.4

We also conducted a comprehensive comparison of the HER FE to relate the surface properties of the nanoporous films to the CO₂RR performance (Figure 4c). The non-BGPF SnO_{0.98}, without a coating layer, shows a lower HER efficiency (10.9-18.7% at -0.7 to -1.1 V) compared to other non-BGPF control samples (e.g., SnO_{1.82}, SnO_{1.33}, and SnO_{1.57}). This implies that the presence of the mixed phase of SnO_{0.98} leads to the lowest selectivity toward H2 production, thereby contributing to a higher partial current density for CO₂RR. Moreover, the measured CA (151.1°, See Figure S12) of SnO_{0.98}, which is considerably higher than that of the other non-BGPF control samples, illustrates its superior gasphilicity resulting from superhydrophobicity. As expected, all SAFM-coated nanoporous films show remarkably reduced hydrogen production compared with their uncoated counterparts. In particular, BGPF displays further enhanced gasphilicity (CA of 158°) and, surprisingly, the lowest HER efficiency (7.5-9.8% at -0.7 to)

-1.1 V), compared to all other control samples. The ability to suppress hydrogen generation while increasing CO₂RR FE underscores the critical role of interface engineering in optimizing CO₂RR performance.

LSV was also utilized to discern the CO2RR selectivity of the samples in N₂- and CO₂-saturated 0.5 M KHCO₃ electrolytes. Within a potential window of -0.7 to -1.1 V, both SAFMcoated and uncoated samples demonstrate higher cathodic current density in the CO2-saturated electrolytes compared to the N₂-saturated electrolytes, confirming their electrocatalytic activity for the CO2RR. However, the LSV current densities of all SAFM-coated samples (e.g., BGPF, SnO_{1,33}-F, SnO_{0,98}-F, and SnO_{1.57}-F) in the CO₂-saturated electrolytes and N₂-saturated are lower than the uncoated ones, suggesting a reduction in the current density associated with HER due to the repulsion of protons from the electrode surface (Figure S28a-d). The LSV curves measured in the N2-saturated electrolytes indicated that the BGPF exhibits the lowest current density related to hydrogen generation, which aligns well with the previously determined low HER FE. Moreover, other SAFM-coated samples (e.g., SnO_{1.82}-F, SnO_{1.33}-F, and SnO_{1.57}-F) display less hydrogen generation compared with their uncoated counterparts, further validating the improvement of gasphilicity through surface coating. In summary, based on all the aforementioned discussions, we have demonstrated that a balance of active phase modulation, morphology control, and surface coating is pivotal for optimizing the triple-phase interface when designing new catalysts for CO₂RR and other applications.^{39,48}

2.5. Mechanistic Understanding of Dynamic Recovery in Active Phase. SnO_x catalysts may undergo surface reconstruction toward metallic tin, a process facilitated by facile Sn-O bond breakage during CO₂RR. This significantly lowers the corresponding FE of CO_2 electrolysis and leads to undesired hydrogen generation. 49-51 Rather than applying constant potentials to the electrode, pulsed electrochemistry using a square-wave potential, composed of specific anodic and cathodic potentials, can dynamically steer reaction products and suppress hydrogen generation for CO₂RR. The applied anodic potential alters the surface properties of the electrode, including the tin chemical state and surface adsorbates, thereby tuning the reaction selectivity. 52-54 We cyclically applied a square-wave potential to BGPF at different cathodic potentials for $\Delta t_c = 30$ s and then at an anodic potential of 0.2 V for $\Delta t_a = 5$ s (Figure S29). As shown in Figure 4d, hydrogen production was exceptionally lower by nearly 4% across all applied potentials from -0.7 to -1.1 V compared to results obtained under constant potentials. This highlights the beneficial role of pulsed potentials in enhancing the possible electroabsorption of hydroxides on the electrode surface at applied anodic potentials. Compared to the CO₂RR performance obtained under constant potentials applied to BGPF, we observed similar CO production but formate production increased by about 5% in the sample tested with pulsed potentials. This indicates that the applied anodic potentials facilitate dynamic recovery of the active phase and regulation of the local microenvironment. Moreover, an electrochemical stability test using cyclically pulsed potentials $(\Delta t_a = 5 \text{ s at } 0.2 \text{ V and } \Delta t_c = 30 \text{ s at } -0.8 \text{ V})$ was performed for 10 h. Strikingly, the formate production FE (\sim 68%) was well maintained under pulsed potentials (Figure 4e), whereas that of formate declined to 56%, accompanied by an increase in hydrogen generation (\sim 5–13%, Figure S30) when tested under a constant potential of -0.8 V. Moreover, a more than 10% increase in the current density retention was obtained when

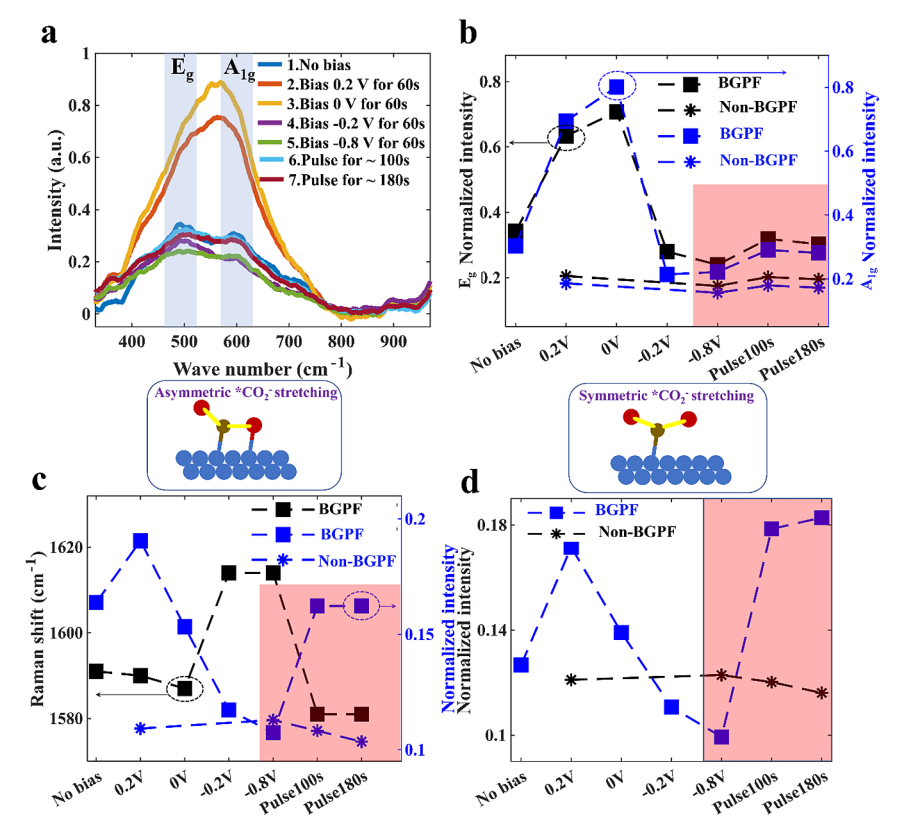


Figure 5. Mechanistic study of the dynamic recovery of the surface-active phase. (a) In situ Raman spectroscopy of BGPF under different electrochemical conditions. (b) Influence of electrochemical potentials on the intensity of E_g and A_{1g} vibrational modes centered around 476 and 623 cm⁻¹, respectively. (c, d) Effect of electrochemical potentials on the intensity and Raman shift of the carboxylate * CO_2 - intermediate, determined from the in situ Raman spectra of BGPF at the specific Raman shift ranges of 1580–1620 and 1335 cm⁻¹, respectively. The shaded areas indicate the regions where the CO_2RR process was observed.

switching from constant to pulsed potential mode (Figure S31). The unaltered nanoporous morphology and well maintained hydrophobic surface were confirmed by SEM (Figure S32) and CA measurements (Figure S33), respectively. Additionally, the presence of the F signal (688.4 eV) after electrochemical tests, as detected by XPS (Figure S34) doubly confirms the robust adherence of the coating layer to the sample surface.

To gain a mechanistic understanding of the function of the pulsed square-wave potentials, particularly the anodic potentials, in tuning the active phase of the sample to enhance the selectivity of the CO₂RR, an in situ Raman technique was used. This allowed us to probe the variations of the vibrational mode under electrochemical conditions. We applied both constant (0.2 and -0.8 V) and cyclically pulsed potentials ($\Delta t_a = 5 \text{ s at } 0.2 \text{ m}$ V and $\Delta t_c = 30$ s at -0.8 V) separately on BGPF and non-BGPF SnO_{1,82}. As shown in Figure 5a, upon application of a constant oxidative potential at 0.2 V for 60 s, we observed a sharp increase in intensity in both E_g (476 cm⁻¹) and A_{1g} (623 cm⁻¹) vibrational modes in BGPF compared to the sample with no bias applied, suggesting that the oxidative potential could induce surface lattice vibration that might be responsible for tuning selective CO₂RR toward desired C1 products.³³ In these two Raman-active modes, the O atoms vibrate in a specific direction, while the Sn atoms remain stationary. This implies that a dynamic oxidative potential can replenish the surface oxygen, potentially maintaining a high oxygen affinity for *OCHO.1 also noticed a rise in the peak intensities mentioned above under pulsed conditions (illustrated by light blue and brown curves in Figure 5a) for BGPF. These peaks are higher than those

observed at the constant potential of -0.8 V (green solid curves in Figure 5a), providing evidence for the superiority of a dynamic potential over a constant potential in recovering the active phase. Figure 5b outlines the changes in the Raman peak intensity of the $E_{\rm g}$ and $A_{\rm lg}$ modes under constant potential and pulsed potentials applied to both BGPF and non-BGPF samples. For BGPF, both E_g and A_{1g} intensities increase upon application of oxidative potentials for BGPF. In addition, these intensities are higher for pulsed working conditions compared to constant potential operation, as highlighted in the shaded area. In contrast, the characteristic peaks for non-BGPF exhibit steady peak intensities across all conditions, indicating no surfacesensitive perturbation of E_g and A_{1g} under oxidative conditions. Conversely, under a constant reductive condition of -0.8 V for 60 s, both BGPF and non-BGPF samples exhibit decreased surface vibrational mode intensity compared to the initial state. This suggests a continuous degradation of the active phase under solely reductive conditions (Figure S35). Moreover, the increased vibrational peak intensity observed for BGPF aligns well with the enhanced formate production FE under pulsed conditions, proving the structure-property relationship for uncovering efficient catalyst design.⁵

We further explored the activation of CO_2 and adsorption of the $^*CO_2^-$ intermediate on the electrode using in situ Raman spectroscopy (Figure S36). This analysis revealed changes in intensity and vibrational frequency of Raman-active intermediates as the potentials were scanned. This is attributed to the electrochemical Stark effect, which relates to the orientation of the adsorbates under an electric field. $^*CO_2^-$ is believed to be

the first intermediate when CO₂RR proceeds toward C₁ products such as formate and CO, thus playing an important role in promoting CO₂RR kinetics.⁵⁵ We plotted the effect of electrochemical potentials on the intensity and Raman shifts of asymmetric ($v_{as}CO_2^{-1}$, ~1600 cm⁻¹) and symmetric (v_sCO2^{-1} , \sim 1335 cm⁻¹) stretching modes of *CO₂⁻ in Figure 5c,d. Our results show that both intensities of $v_{as}CO_2^{-1}$ and $v_sCO_2^{-1}$ are highest at 0.2 V, where the CO₂ reduction has not occurred, originating from the adsorption of CO₂ in the electrolyte. As the potential scanned negatively to the representative working potential of -0.8 V for BGPF (blue square labeled dashed curve in Figure 5c,d), the intensity of *CO2 is greatly reduced, indicating the consumption of *CO₂ on the electrode under reductive conditions. Moreover, the $v_{as}CO_2^{-1}$ peak undergoes a redshift from 0.2 to -0.8 V, which is attributed to the Stark shift effect due to variations in local electric fields (black square labeled dashed curve in Figure 5c), reflecting the potentialdependent chemisorbed state of the intermediate. Under pulsed conditions, the intensity of *CO₂⁻ remains higher than under the constant potential (shown in the shaded area), which can be attributed to the dynamic recovery of the active phase of the catalyst and valid anodic potential for the generation of $*CO_2^{-25,56}$. In contrast, non-BGPF samples did not display obvious changes in intensity or frequency under any conditions (blue-asterisk-labeled dashed curve in Figure 5c and blackasterisk-labeled dashed curve in Figure 5d), further confirming the significance of maintaining an appropriate phase composition for enhancing CO₂RR activity and long-term stability.

3. CONCLUSIONS

We present a rationally designed bioinspired gasphilic SnO_x nanoporous film electrode to regulate the microenvironment at the triple-phase interface during CO₂RR. Through thermal annealing, we established an optimized mixed thermodynamic phase of amorphous SnO and polycrystalline SnO₂ within the nanoporous film, facilitating the selective conversion of CO₂ to advantageous C1 products such as formate and CO. Additionally, an SAFM-coating was applied to the nanoporous film to further modify the local microenvironment at the triple-phase interface, resulting in an unconventional "plastron"-like layer in water. This nanoporous film demonstrated the ability to selfcapture CO₂ at the modified triple-phase interface in a CO₂saturated electrolyte. This approach increases the local CO₂ concentration, overcoming the issue of limited CO₂ solubility. Furthermore, we adopted a technique that employs pulsed square-wave potentials to direct the CO₂RR conversion toward the preferred formate product and ensure long-term stable CO₂RR activity. With in situ Raman spectroscopy, we identified clear potential-dependent shifts and variations in intensity for vibrational modes of E_g and A_{1g} in $SnO_{0.98}$ -F and the first CO_2 intermediate, underscoring the critical role of dynamic recovery of the active phase in maintaining stable CO₂RR. As a result, we achieved a stable CO2RR FE of ~85% throughout a 10 h duration in pulsed conditions. Our study validates the synergistic application of interface engineering for controlling the critical triple-phase interface for the CO₂RR and beyond, providing insights for catalyst design in emerging electrochemical processes aimed at electrification and decarbonization.

ASSOCIATED CONTENT

Supporting Information

The Supporting Information is available free of charge at https://pubs.acs.org/doi/10.1021/jacs.4c02786.

Water droplet sliding experiment on the BGPF electrode (AVI)

Animated illustration of water droplet sliding experiment on the BGPF electrode (AVI)

Animated illustration of CO₂RR process on the BGPF electrode, CO₂ gas is captured by the BGPF followed by nucleation, growth, and bubbling (AVI)

Surface morphology state of BGPF under water after CV scan during CO₂RR process (AVI)

Frame subtracted surface morphology state of BGPF under water after CV scan during CO₂RR process (AVI) Frame subtracted surface morphology state of BGPF under water @0 V during CO₂RR process (AVI)

Frame subtracted surface morphology state of BGPF under water @-0.2 V during CO₂RR process (AVI)

Frame subtracted surface morphology state of BGPF under water @-0.4 V during CO₂RR process (AVI)

Frame subtracted surface morphology state of BGPF under water @-0.6 V during CO₂RR process (AVI)

Frame subtracted surface morphology state of BGPF under water @-0.8 V during CO₂RR process (AVI)

Frame subtracted surface morphology state of BGPF under water @-1 V during CO₂RR process (AVI)

Surface morphology state of non-BGPF under water after CV scan during CO₂RR process (AVI)

Surface morphology state of non-BGPF under water @ -0.2 V during CO₂RR process (AVI)

Frame subtracted surface morphology state of non-BGPF under water @-0.2 V during CO₂RR process (AVI)

Frame subtracted surface morphology state of non-BGPF under water @-0.8 V during CO2RR process (AVI)

Experimental section; elaboration on biomimetic inspiration; cross-sectional SEM image of BGPF electrode; TEM diffraction pattern of SnO_{1.82}, corresponding HAADF image, EDS elemental mapping of Sn and O as well as atomic ratio; TEM diffraction pattern of SnO_{1.33}, corresponding HAADF image and EDS elemental mapping of Sn and O as well as atomic ratio; TEM-HAADF image of SnO_{0.98}, interplanar spacing of local SnO₂, HAADF image and EDS elemental mapping of Sn and O as well as atomic ratio; STEM-HAADF image of SnO_{1.57} amorphous region, polycrystalline region, HAADF image and EDS elemental mapping of Sn and O as well as the atomic ratio; XRD patterns of SnO_{1.82}, SnO_{1.33}, SnO_{0.98}, and SnO_{1.57}; XPS O 1s spectra of non-SAFM-coated SnO_{0.98}, Si 2p, and F 1s spectra of BGPF, C 1s spectra comparison of BGPF, and non-SAFM-coated SnO_{0.98}; XPS survey spectra of BGPF and non-SAFMcoated SnO_{0.98}; "plastron" effect achieved in the BGPF electrode when immersed in water; surface roughness and max height level of BGPF electrode revealed from confocal laser scanning microscopy; O 1s XPS of BGPF and non-BGPF SnO_{1.82}; CAs of all the BGPF and non-BGPF cases; SEM images of SnO_{1.82}, SnO_{1.33}, BGPF, and SnO_{1.57}; surface roughness and max height level of non-BGPF electrode revealed from confocal laser scanning microscopy; variations of the roughness of all the samples; morphological image of BGPF and non-BGPF SnO₁₈₂ electrode in 0.5 M K_HCO₃ electrolyte; CO₂ self-capturing concentration of BGPF under different constant potentials during CO₂RR; bubble self-capturing property of BGPF under different constant potentials; electrochemical active surface area estimation of BGPF, nonBGPFs of $SnO_{1.82}$, $SnO_{1.33}$, $SnO_{0.98}$, and $SnO_{1.57}$; comparison of LSV curves for different electrodes during OER, i-t curves of different electrodes under a constant current density of 5 mA/cm² for OER; CV curves of BGPF in CO₂- and N₂-saturated 0.5 M K_HCO₃ electrolytes; chronoamperometry i-t curves of SnO_{1.82-F}, SnO_{1.33-F}, BGPF, SnO_{1.57-F}, SnO_{1.82}, SnO_{1.33}, SnO_{0.98}, SnO_{1.57}; gas chromatography curves used for determining the efficiency of hydrogen and CO production; NMR spectrum of the cathodic analyte after CO2RR stability test of BGPF and NMR calibration curves of formate with various concentrations; effective CO₂RR current density plot of BGPF, SnO_{1.82-F}, SnO_{1,33-F}, SnO_{1,57-F}, and SnO_{1,82}, SnO_{1,33}, SnO_{0,98}, and SnO_{1.57} under different constant potentials; CO₂RR FE of SnOx flat electrode under different constant potentials; CO₂RR FE of SnO_{1.82}, SnO_{1.82-F}, SnO_{1.33}, SnO_{1.33-F}, $SnO_{0.98}$, BGPF, $SnO_{1.57}$, and $SnO_{1.57\text{-F}}$ under different constant potentials; LSV curves of all SAFM-coated porous films and uncoated porous films in CO2-saturated 0.5 M K_HCO₃, SAFM-coated porous films and uncoated porous films in N2-saturated 0.5 M KHCO3 electrolyte; i-t curves of BGPF under square-wave pulsed potentials during CO₂RR; CO₂RR FE of BGPF; i-t curves of BGPF under square-wave pulsed potentials during a 10 h CO₂RR stability test; cross-sectional and top-view SEM image of reacted BGPF after a 10 h stability test under pulsed square-wave potentials; water CA and water droplet pull-off experiment of reacted BGPF after a 10 h stability test under pulsed square-wave potentials; XPS F 1s spectra of BGPF after a 10 h stability test under pulsed square-wave potentials; in situ Raman spectra of BGPF and non-BGPF of SnO_{1.82} under different electrochemical conditions during CO2RR; in situ Raman spectroscopy of BGPF under different electrochemical conditions for intermediate *CO2- at specific wavenumber range of 1580-1620 cm⁻¹ and 1335 cm⁻¹ (PDF)

AUTHOR INFORMATION

Corresponding Authors

- Jeffrey A. Reimer Department of Chemical and Biomolecular Engineering, University of California, Berkeley, Berkeley, California 94720, United States; Materials Sciences Division, Lawrence Berkeley National Laboratory, Berkeley, California 94720, United States; Email: reimer@berkeley.edu
- Yi Cui Department of Materials Science and Engineering, Stanford University, Stanford, California 94305, United States; orcid.org/0000-0002-6103-6352; Email: yicui@stanford.edu
- Yang Yang NanoScience Technology Center, Department of Materials Science and Engineering, Renewable Energy and Chemical Transformation Cluster, Department of Chemistry, and The Stephen W. Hawking Center for Microgravity Research and Education, University of Central Florida, Orlando, Florida 32826, United States; ocid.org/0000-0002-4410-6021; Email: Yang, Yang@ucf.edu

Authors

Wei Zhang — NanoScience Technology Center and Department of Materials Science and Engineering, University of Central Florida, Orlando, Florida 32826, United States; orcid.org/0000-0002-7846-8063

- Ao Yu NanoScience Technology Center, University of Central Florida, Orlando, Florida 32826, United States; orcid.org/0000-0003-1449-6329
- Haiyan Mao Department of Materials Science and Engineering, Stanford University, Stanford, California 94305, United States; Department of Chemical and Biomolecular Engineering, University of California, Berkeley, Berkeley, California 94720, United States
- Guangxia Feng Electrical and Computer Engineering Department, University of Houston, Houston, Texas 77204, United States
- Cheng Li Eastern Institute for Advanced Study, Eastern Institute of Technology, Ningbo, Zhejiang 315200, P.R. China; School of Physics and Astronomy, University of Birmingham, Birmingham B15 2TT, U.K.
- Guanzhi Wang NanoScience Technology Center and Department of Materials Science and Engineering, University of Central Florida, Orlando, Florida 32826, United States; orcid.org/0000-0002-5094-5630
- Jinfa Chang NanoScience Technology Center, University of Central Florida, Orlando, Florida 32826, United States; Faculty of Chemistry, Key Laboratory of Polyoxometalate and Reticular Material Chemistry of Ministry of Education, Northeast Normal University, Changchun 130024, P.R. China; orcid.org/0000-0002-5066-3625
- David Halat Department of Chemical and Biomolecular Engineering, University of California, Berkeley, Berkeley, California 94720, United States; ⊙ orcid.org/0000-0002-0919-1689
- **Zhao Li** NanoScience Technology Center and Department of Materials Science and Engineering, University of Central Florida, Orlando, Florida 32826, United States
- Weilai Yu Department of Materials Science and Engineering, Stanford University, Stanford, California 94305, United States; ocid.org/0000-0002-9420-0702
- Yaping Shi Electrical and Computer Engineering Department, University of Houston, Houston, Texas 77204, United States
- Shengwen Liu NanoScience Technology Center, University of Central Florida, Orlando, Florida 32826, United States
- David W. Fox NanoScience Technology Center and Department of Chemistry, University of Central Florida, Orlando, Florida 32826, United States
- Hao Zhuang Department of Chemical and Biomolecular Engineering, University of California, Berkeley, Berkeley, California 94720, United States
- **Angela Cai** Department of Materials Science and Engineering, Stanford University, Stanford, California 94305, United States
- Bing Wu Department of Chemical and Biomolecular Engineering, University of California, Berkeley, Berkeley, California 94720, United States; ⊚ orcid.org/0000-0002-2739-5124
- Fnu Joshua NanoScience Technology Center, University of Central Florida, Orlando, Florida 32826, United States
- John R. Martinez Department of Chemistry, University of Central Florida, Orlando, Florida 32826, United States
- Lei Zhai NanoScience Technology Center and Department of Chemistry, University of Central Florida, Orlando, Florida 32826, United States; orcid.org/0000-0002-3886-2154
- M. Danny Gu − Eastern Institute for Advanced Study, Eastern Institute of Technology, Ningbo, Zhejiang 315200, P.R. China; © orcid.org/0000-0002-5126-9611

Xiaonan Shan — Electrical and Computer Engineering
Department, University of Houston, Houston, Texas 77204,
United States; orcid.org/0000-0001-7521-5573

Complete contact information is available at: https://pubs.acs.org/10.1021/jacs.4c02786

Author Contributions

W.Z., A.Y., and H. M. contributed equally to the manuscript. All authors approved the manuscript.

Notes

The authors declare no competing financial interest.

ACKNOWLEDGMENTS

This work was supported by the National Science Foundation under Grant Nos. CMMI-1851674, CBET-1949840, and ACS PRF (65481-ND10). The XPS characterization was supported by the National Science Foundation NSF MRI: XPS: ECCS: 1726636, hosted in the MCF-AMPAC facility, MSE, CECS, and UCF. X.S. acknowledges the funding support from the USDA SBIR award (No. 2022-70012-36900 and 2019-33610-29769), University Training and Research for Fossil Energy Applications (DOE DE-FE-0032092), and the UL Research Institutes. The Raman characterization was supported by the National Science Foundation under Grant No. DMR 1920050 (MRI). The solidstate-NMR characterization was partly supported by the DOE, Office of Basic Energy Sciences, Division of Materials Sciences and Engineering (contract no. DE-AC02-76SF00515). J.A.R. acknowledges partial support from the ACT-PrISMa project, which has received joint funding from BEIS, NERC, and EPSRC (UK), funding from the Division of CCS R&D, DOE, and funding from the Office Fédéral de l'Energie (Switzerland).

■ REFERENCES

- (1) Hepburn, C.; Adlen, E.; Beddington, J.; Carter, E. A.; Fuss, S.; Mac Dowell, N.; Minx, J. C.; Smith, P.; Williams, C. K. The technological and economic prospects for CO_2 utilization and removal. *Nature* **2019**, 575 (7781), 87–97.
- (2) Rogelj, J.; Geden, O.; Cowie, A.; Reisinger, A. Net-zero emissions targets are vague: three ways to fix. *Nature* **2021**, *591* (7850), 365–368.
- (3) Grim, R. G.; Huang, Z.; Guarnieri, M. T.; Ferrell, J. R.; Tao, L.; Schaidle, J. A. Transforming the carbon economy: challenges and opportunities in the convergence of low-cost electricity and reductive CO₂ utilization. *Energy Environ. Sci.* **2020**, 13 (2), 472–494.
- (4) Pan, F.; Yang, Y. Designing CO_2 reduction electrode materials by morphology and interface engineering. *Energy Environ. Sci.* **2020**, *13* (8), 2275–2309.
- (5) Li, Z.; Cao, A.; Zheng, Q.; Fu, Y.; Wang, T.; Arul, K. T.; Chen, J.-L.; Yang, B.; Adli, N. M.; Lei, L.; Dong, C.-L.; Xiao, J.; Wu, G.; Hou, Y. Elucidation of the Synergistic Effect of Dopants and Vacancies on Promoted Selectivity for CO_2 Electroreduction to Formate. *Adv. Mater.* **2021**, 33 (2), No. 2005113.
- (6) Kibria, M. G.; Edwards, J. P.; Gabardo, C. M.; Dinh, C.-T.; Seifitokaldani, A.; Sinton, D.; Sargent, E. H. Electrochemical CO₂ Reduction into Chemical Feedstocks: From Mechanistic Electrocatalysis Models to System Design. *Adv. Mater.* **2019**, *31* (31), No. 1807166.
- (7) Song, J. T.; Ryoo, H.; Cho, M.; Kim, J.; Kim, J.-G.; Chung, S.-Y.; Oh, J. Nanoporous Au Thin Films on Si Photoelectrodes for Selective and Efficient Photoelectrochemical CO₂ Reduction. *Adv. Energy Mater.* **2017**, *7* (3), No. 1601103.
- (8) Gu, J.; Héroguel, F.; Luterbacher, J.; Hu, X. Densely Packed, Ultra Small SnO Nanoparticles for Enhanced Activity and Selectivity in Electrochemical CO₂ Reduction. *Angew. Chem., Int. Ed.* **2018**, *57* (11), 2943–2947.

- (9) Kumar, B.; Atla, V.; Brian, J. P.; Kumari, S.; Nguyen, T. Q.; Sunkara, M.; Spurgeon, J. M. Reduced SnO₂ Porous Nanowires with a High Density of Grain Boundaries as Catalysts for Efficient Electrochemical CO₂-into-HCOOH Conversion. *Angew. Chem., Int. Ed.* **2017**, *56* (13), 3645–3649.
- (10) Fan, L.; Xia, Z.; Xu, M.; Lu, Y.; Li, Z. 1D SnO₂ with Wire-in-Tube Architectures for Highly Selective Electrochemical Reduction of CO₂ to C₁ Products. *Adv. Funct. Mater.* **2018**, 28 (17), No. 1706289.
- (11) Liu, G.; Li, Z.; Shi, J.; Sun, K.; Ji, Y.; Wang, Z.; Qiu, Y.; Liu, Y.; Wang, Z.; Hu, P. Black reduced porous SnO₂ nanosheets for CO₂ electroreduction with high formate selectivity and low overpotential. *Appl. Catal. B: Environ.* **2020**, *260*, No. 118134.
- (12) Li, F.; Chen, L.; Knowles, G. P.; MacFarlane, D. R.; Zhang, J. Hierarchical Mesoporous SnO₂ Nanosheets on Carbon Cloth: A Robust and Flexible Electrocatalyst for CO₂ Reduction with High Efficiency and Selectivity. *Angew. Chem., Int. Ed.* **2017**, *56* (2), 505–509.
- (13) Baruch, M. F.; Pander, J. E., III; White, J. L.; Bocarsly, A. B. Mechanistic Insights into the Reduction of CO₂ on Tin Electrodes using in Situ ATR-IR Spectroscopy. *ACS Catal.* **2015**, *5* (5), 3148–3156.
- (14) Zhang, W.; Chang, J.; Yang, Y. Strong precious metal—metal oxide interaction for oxygen reduction reaction: A strategy for efficient catalyst design. *SusMat* **2023**, 3 (1), 2–20.
- (15) Salvini, C.; Re Fiorentin, M.; Risplendi, F.; Raffone, F.; Cicero, G. Active Surface Structure of SnO₂ Catalysts for CO₂ Reduction Revealed by Ab Initio Simulations. *J. Phys. Chem. C* **2022**, *126* (34), 14441–14447.
- (16) Lee, S. H.; Lin, J. C.; Farmand, M.; Landers, A. T.; Feaster, J. T.; Avilés Acosta, J. E.; Beeman, J. W.; Ye, Y.; Yano, J.; Mehta, A.; Davis, R. C.; Jaramillo, T. F.; Hahn, C.; Drisdell, W. S. Oxidation State and Surface Reconstruction of Cu under CO₂ Reduction Conditions from In Situ X-ray Characterization. *J. Am. Chem. Soc.* **2021**, *143* (2), 588–592.
- (17) Lai, W.; Ma, Z.; Zhang, J.; Yuan, Y.; Qiao, Y.; Huang, H. Dynamic Evolution of Active Sites in Electrocatalytic CO₂ Reduction Reaction: Fundamental Understanding and Recent Progress. *Adv. Funct. Mater.* **2022**, 32 (16), No. 2111193.
- (18) Ross, M. B.; De Luna, P.; Li, Y.; Dinh, C.-T.; Kim, D.; Yang, P.; Sargent, E. H. Designing materials for electrochemical carbon dioxide recycling. *Nature Catal.* **2019**, *2* (8), 648–658.
- (19) Gao, D.; Arán-Ais, R. M.; Jeon, H. S.; Roldan Cuenya, B. Rational catalyst and electrolyte design for CO₂ electroreduction towards multicarbon products. *Nature Catal.* **2019**, 2 (3), 198–210.
- (20) Kothary, P.; Dou, X.; Fang, Y.; Gu, Z.; Leo, S.-Y.; Jiang, P. Superhydrophobic hierarchical arrays fabricated by a scalable colloidal lithography approach. *J. Colloid Interface Sci.* **2017**, *487*, 484–492.
- (21) Niu, Z.-Z.; Gao, F.-Y.; Zhang, X.-L.; Yang, P.-P.; Liu, R.; Chi, L.-P.; Wu, Z.-Z.; Qin, S.; Yu, X.; Gao, M.-R. Hierarchical Copper with Inherent Hydrophobicity Mitigates Electrode Flooding for High-Rate CO₂ Electroreduction to Multicarbon Products. *J. Am. Chem. Soc.* **2021**, 143 (21), 8011–8021.
- (22) Ma, M.; Djanashvili, K.; Smith, W. A. Controllable Hydrocarbon Formation from the Electrochemical Reduction of CO₂ over Cu Nanowire Arrays. *Angew. Chem., Int. Ed.* **2016**, *55* (23), 6680–6684.
- (23) Yang, B.; Liu, K.; Li, H.; Liu, C.; Fu, J.; Li, H.; Huang, J. E.; Ou, P.; Alkayyali, T.; Cai, C.; Duan, Y.; Liu, H.; An, P.; Zhang, N.; Li, W.; Qiu, X.; Jia, C.; Hu, J.; Chai, L.; Lin, Z.; Gao, Y.; Miyauchi, M.; Cortés, E.; Maier, S. A.; Liu, M. Accelerating CO₂ Electroreduction to Multicarbon Products via Synergistic Electric—Thermal Field on Copper Nanoneedles. *J. Am. Chem. Soc.* **2022**, *144* (7), 3039–3049.
- (24) Liu, M.; Pang, Y.; Zhang, B.; De Luna, P.; Voznyy, O.; Xu, J.; Zheng, X.; Dinh, C. T.; Fan, F.; Cao, C.; de Arquer, F. P. G.; Safaei, T. S.; Mepham, A.; Klinkova, A.; Kumacheva, E.; Filleter, T.; Sinton, D.; Kelley, S. O.; Sargent, E. H. Enhanced electrocatalytic CO₂ reduction via field-induced reagent concentration. *Nature* **2016**, *537* (7620), 382–386.

- (25) Chernyshova, I. V.; Somasundaran, P.; Ponnurangam, S. On the origin of the elusive first intermediate of CO₂ electroreduction. *Proc. Natl. Acad. Sci. U. S. A.* **2018**, *115* (40), E9261–E9270.
- (26) Atrak, N.; Tayyebi, E.; Skúlason, E. Insight into Catalytic Active Sites on TiO₂/RuO₂ and SnO₂/RuO₂ Alloys for Electrochemical CO₂ Reduction to CO and Formic Acid. *ACS Catal.* **2023**, *13*, 5491–5501.
- (27) Hsu, P.-C.; Hsu, C.-J.; Chang, C.-H.; Tsai, S.-P.; Chen, W.-C.; Hsieh, H.-H.; Wu, C.-C. Sputtering Deposition of P-Type SnO Films with SnO₂ Target in Hydrogen-Containing Atmosphere. *ACS Appl. Mater. Interfaces* **2014**, *6* (16), 13724–13729.
- (28) Meng, L.; Bu, W.; Li, Y.; Qin, Q.; Zhou, Z.; Hu, C.; Chuai, X.; Wang, C.; Sun, P.; Lu, G. Highly selective triethylamine sensing based on SnO/SnO₂ nanocomposite synthesized by one-step solvothermal process and sintering. *Sens. Actuators B: Chem.* **2021**, 342, No. 130018.
- (29) Du, W.; Liu, M.; Han, F.; Su, H.; Zhang, H.; Liu, B.; Meng, H.; Tang, X. Role of oxygen migration on the thermal stability of the perpendicular magnetic anisotropy in bottom and top structures. *APL Mater.* **2022**, *10* (1), No. 011101.
- (30) Ren, Z.; Ng, A.; Shen, Q.; Gokkaya, H. C.; Wang, J.; Yang, L.; Yiu, W.-K.; Bai, G.; Djurišić, A. B.; Leung, W. W.-F.; Hao, J.; Chan, W. K.; Surya, C. Thermal Assisted Oxygen Annealing for High Efficiency Planar CH₃NH₃PbI₃ Perovskite Solar Cells. *Sci. Rep.* **2014**, *4* (1), 6752.
- (31) Diéguez, A.; Romano-Rodríguez, A.; Morante, J. R.; Weimar, U.; Schweizer-Berberich, M.; Göpel, W. Morphological analysis of nanocrystalline SnO₂ for gas sensor applications. *Sens. Actuators B: Chem.* 1996, 31 (1), 1–8.
- (32) Vijayarangamuthu, K.; Rath, S. Nanoparticle size, oxidation state, and sensing response of tin oxide nanopowders using Raman spectroscopy. *J. Alloys Compd.* **2014**, *610*, 706–712.
- (33) Diéguez, A.; Romano-Rodríguez, A.; Vilà, A.; Morante, J. R. The complete Raman spectrum of nanometric SnO₂ particles. *J. Appl. Phys.* **2001**, *90* (3), 1550–1557.
- (34) Shen, X.; Nagai, T.; Yang, F.; Zhou, L. Q.; Pan, Y.; Yao, L.; Wu, D.; Liu, Y.-S.; Feng, J.; Guo, J.; Jia, H.; Peng, Z. Dual-Site Cascade Oxygen Reduction Mechanism on SnO_x/Pt-Cu-Ni for Promoting Reaction Kinetics. *J. Am. Chem. Soc.* **2019**, *141* (24), 9463–9467.
- (35) Yamamoto, S.; Bluhm, H.; Andersson, K.; Ketteler, G.; Ogasawara, H.; Salmeron, M.; Nilsson, A. In situ x-ray photoelectron spectroscopy studies of water on metals and oxides at ambient conditions. *J. Condens. Matter Phys.* **2008**, *20* (18), No. 184025.
- (36) Lee, B.; Chen, Y.; Duerr, F.; Mastrogiovanni, D.; Garfunkel, E.; Andrei, E. Y.; Podzorov, V. Modification of Electronic Properties of Graphene with Self-Assembled Monolayers. *Nano Lett.* **2010**, *10* (7), 2427–2432.
- (37) Flynn, M. R.; Bush, J. W. M. Underwater breathing: the mechanics of plastron respiration. *J. Fluid Mech.* **2008**, 608, 275–296.
- (38) Trogadas, P.; Coppens, M.-O. Nature-inspired electrocatalysts and devices for energy conversion. *Chem. Soc. Rev.* **2020**, 49 (10), 3107–3141.
- (39) Iwata, R.; Zhang, L.; Wilke, K. L.; Gong, S.; He, M.; Gallant, B. M.; Wang, E. N. Bubble growth and departure modes on wettable/nonwettable porous foams in alkaline water splitting. *Joule* **2021**, *5* (4), 887–900.
- (40) Xing, Z.; Hu, L.; Ripatti, D. S.; Hu, X.; Feng, X. Enhancing carbon dioxide gas-diffusion electrolysis by creating a hydrophobic catalyst microenvironment. *Nat. Commun.* **2021**, *12* (1), 136.
- (41) Shi, R.; Guo, J.; Zhang, X.; Waterhouse, G. I. N.; Han, Z.; Zhao, Y.; Shang, L.; Zhou, C.; Jiang, L.; Zhang, T. Efficient wettability-controlled electroreduction of CO₂ to CO at Au/C interfaces. *Nat. Commun.* **2020**, *11* (1), 3028.
- (42) Angulo, A.; van der Linde, P.; Gardeniers, H.; Modestino, M.; Fernández Rivas, D. Influence of Bubbles on the Energy Conversion Efficiency of Electrochemical Reactors. *Joule* **2020**, *4* (3), 555–579.
- (43) Panchanathan, D.; Rajappan, A.; Varanasi, K. K.; McKinley, G. H. Plastron Regeneration on Submerged Superhydrophobic Surfaces Using In Situ Gas Generation by Chemical Reaction. *ACS Appl. Mater. Interfaces* **2018**, *10* (39), 33684–33692.
- (44) Verho, T.; Korhonen, J. T.; Sainiemi, L.; Jokinen, V.; Bower, C.; Franze, K.; Franssila, S.; Andrew, P.; Ikkala, O.; Ras, R. H. A. Reversible

- switching between superhydrophobic states on a hierarchically structured surface. *Proc. Natl. Acad. Sci. U. S. A.* **2012**, *109* (26), 10210–10213.
- (45) Khan, S.; Hwang, J.; Horn, Y.-S.; Varanasi, K. K. Catalyst-proximal plastrons enhance activity and selectivity of carbon dioxide electroreduction. *Cell Rep. Phys. Sci.* **2021**, 2 (2), No. 100318.
- (46) Li, J.; Chen, G.; Zhu, Y.; Liang, Z.; Pei, A.; Wu, C.-L.; Wang, H.; Lee, H. R.; Liu, K.; Chu, S.; Cui, Y. Efficient electrocatalytic CO₂ reduction on a three-phase interface. *Nat. Catal.* **2018**, *1* (8), 592–600. (47) De Luna, P.; Quintero-Bermudez, R.; Dinh, C.-T.; Ross, M. B.;
- Bushuyev, O. S.; Todorović, P.; Regier, T.; Kelley, S. O.; Yang, P.; Sargent, E. H. Catalyst electro-redeposition controls morphology and oxidation state for selective carbon dioxide reduction. *Nat. Catal.* **2018**, *1* (2), 103–110.
- (48) Zhang, W.; Chang, J.; Wang, G.; Li, Z.; Wang, M.; Zhu, Y.; Li, B.; Zhou, H.; Wang, G.; Gu, M.; Feng, Z.; Yang, Y. Surface oxygenation induced strong interaction between Pd catalyst and functional support for zinc—air batteries. *Energy Environ. Sci.* **2022**, *15* (4), 1573—1584.
- (49) Handoko, A. D.; Wei, F.; Jenndy; Yeo, B. S.; Seh, Z. W. Understanding heterogeneous electrocatalytic carbon dioxide reduction through operando techniques. *Nat. Catal.* **2018**, *1* (12), 922–934.
- (50) Dutta, A.; Kuzume, A.; Rahaman, M.; Vesztergom, S.; Broekmann, P. Monitoring the Chemical State of Catalysts for CO2 Electroreduction: An In Operando Study. *ACS Catal.* **2015**, 5 (12), 7498–7502.
- (51) Wang, P.; Qiao, M.; Shao, Q.; Pi, Y.; Zhu, X.; Li, Y.; Huang, X. Phase and structure engineering of copper tin heterostructures for efficient electrochemical carbon dioxide reduction. *Nat. Commun.* **2018**, *9* (1), 4933.
- (52) Casebolt, R.; Levine, K.; Suntivich, J.; Hanrath, T. Pulse check: Potential opportunities in pulsed electrochemical CO2 reduction. *Joule* **2021**, *5* (8), 1987–2026.
- (53) Timoshenko, J.; Bergmann, A.; Rettenmaier, C.; Herzog, A.; Arán-Ais, R. M.; Jeon, H. S.; Haase, F. T.; Hejral, U.; Grosse, P.; Kühl, S.; Davis, E. M.; Tian, J.; Magnussen, O.; Roldan Cuenya, B. Steering the structure and selectivity of CO₂ electroreduction catalysts by potential pulses. *Nat. Catal.* **2022**, *5* (4), 259–267.
- (54) Kim, C.; Weng, L.-C.; Bell, A. T. Impact of Pulsed Electrochemical Reduction of CO2 on the Formation of C2+ Products over Cu. *ACS Catal.* **2020**, *10* (21), 12403–12413.
- (55) Wuttig, A.; Yaguchi, M.; Motobayashi, K.; Osawa, M.; Surendranath, Y. Inhibited proton transfer enhances Au-catalyzed CO₂-to-fuels selectivity. *Proc. Natl. Acad. Sci. U. S. A.* **2016**, *113* (32), E4585–E4593.
- (56) Fried, S. D.; Boxer, S. G. Measuring Electric Fields and Noncovalent Interactions Using the Vibrational Stark Effect. *Acc. Chem. Res.* **2015**, *48* (4), 998–1006.